NANO LETTERS

pubs.acs.org/NanoLett Letter

Mode-Specific Coupling of Nanoparticle-on-Mirror Cavities with Cylindrical Vector Beams

Valeria Vento, Philippe Roelli,* Sachin Verlekar, and Christophe Galland*

Cite This: *Nano Lett.* 2023, 23, 4885−4892 Read Online

ACCESS | Metrics & More | Article Recommendations | Supporting Information

ABSTRACT: Nanocavities formed by ultrathin metallic gaps permit the reproducible engineering and enhancement of light−matter interaction, with mode volumes reaching the smallest values allowed by quantum mechanics. While the enhanced vacuum field in metallic nanogaps has been firmly evidenced, fewer experimental reports have examined the far-field to near-field input coupling under strongly focused laser beam. Here, we experimentally demonstrate selective excitation of nanocavity modes controlled by the polarization and frequency of the laser beam. We reveal mode selectivity by recording confocal maps of Raman scattering excited by cylindrical vector beams, which are compared to the known excitation near-field patterns. Our measurements reveal the transverse vs longitudinal polarization of the excited antenna mode and how the input coupling rate depends on laser wavelength. The method introduced here is easily applicable to other experimental scenarios, and our results help connect far-field with near-field parameters in quantitative models of nanocavity-enhanced phenomena.

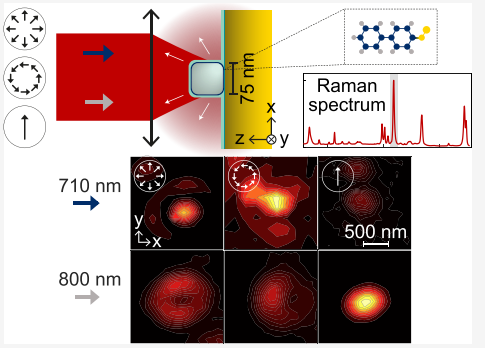

KEYWORDS: *Plasmonic cavities, Plasmonic antennas, Near-field, Cylindrical vector beams, Surface-enhanced Raman scattering*

INTRODUCTION

Plasmonic nanocavities are capable of capturing and confining light in dimensions much smaller than the free-space wavelength, where optically active materials can be positioned. Light−matter interaction is thereby greatly enhanced; when its rate overcomes all intrinsic dissipation rates, the strong-coupling regime can be reached.[1−5] More broadly, plasmonic nanocavities have become instrumental in a number cutting-edge technologies: tip-enhanced Raman spectroscopy (TERS);[6,7] chemistry[8] and electroluminescence[9] at the single molecule limit; enhanced nonlinearities;[10] single-photon sources;[11] coherent frequency upconversion.[12] A common challenge for most applications is to achieve efficient coupling between a traveling electromagnetic wave (the far-field) and a confined plasmonic nanocavity mode (the near-field).[13,14] To this aim, precise knowledge of the spectral and spatial distributions of the plasmonic modes is required as well as techniques to identify, tune, and optimize the coupling from far field radiation to specific subwavelength cavity modes.

Among many different geometries studied in the literature, nanoparticle-on-mirror (NPoM) structures[15,16] constitute versatile, robust, reproducible, and easy-to-fabricate plasmonic nanocavities with intrinsic antenna functionality,[13,14] enabling degrees of confinement and enhancement of optical fields reaching their fundamental limits.[17] The NPoM optical resonances have been classified as transverse waveguide (S) and antenna (L) modes, which typically mix to form hybridized (J) gap modes presenting distinct near-field distributions and far-field radiation patterns.[18−22] Rigorous quantization of these highly dissipative modes and definition of their mode volumes have also been developed in the framework of non hermitian quasi-normal modes.[23,24]

Because near-field intensities for all gap modes are tightly confined within the spacer material, direct and quantitative analysis via near-field scanning probe or electron energy loss spectroscopy has not been achieved. Consequently, experiments rely on elastic dark-field scattering spectra obtained under quasi-plane wave excitation to infer the nanocavity spectrum and which mode is excited at a particular laser wavelength.[20,25] Not only is this approach underestimating or neglecting the contribution of "dark" modes (which do not couple well to incident plane waves but can be efficiently excited by scatterers or emitters in the near field), it is also unable to make prediction as to the relative input coupling rate of a strongly focused laser beam to a particular mode, which can depend not only on laser wavelength but also on the near field polarization at the focus.[26−30] Knowledge of the cavity input coupling rate is required to infer the intracavity excitation number, which in turns govern all optically driven processes in

Received: February 12, 2023
Revised: May 4, 2023
Published: May 19, 2023

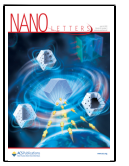

https://doi.org/10.1021/acs.nanolett.3c00561
Nano Lett. 2023, 23, 4885−4892

various applications including surface-enhanced Raman spectroscopy (SERS), photochemistry and photocatalysis, plasmon-enhanced luminescence, nonlinear optics, and frequency conversion. Its role and physical meaning has been evidenced using various formalisms: indirectly via quantum master equations,[31,32] in plasmon induced transparency,[33−36] and also in the context of molecular cavity optomechanics,[37−41] which aims at a more complete description of vibrational and plasmonic correlations and dynamics in SERS. Recent theoretical developments have moreover pointed out its importance for a correct estimate of dissipative coupling rates.[42]

Here, we present a simple and efficient method to determine which nanocavity modes are effectively excited depending on adjustable laser wavelength and polarization. We record the SERS intensity from molecules embedded in NPoM structures under tightly focused radially, azimuthally, and linearly polarized excitation as a function of the NPoM position within the laser focus. We show that the intensity of the SERS signal is typically dominated by the coupling between a single vectorial component of the incoming light field and a single plasmonic gap mode. We demonstrate that polarization and wavelength tuning of the excitation beam allow us to address specific ultraconfined plasmonic modes. Finally, we prove the flexibility of our technique on different plasmonic structures, whose resonances cannot be easily identified with elastic dark-field scattering. We anticipate that our method will help understanding, modeling, and optimizing mode-specific excitation and in-coupling efficiency for a broad range of nanocavities, thus boosting further the desired light−matter interaction while reducing unwanted effects such as Joule heating, and unlocking the full potential of multimode photonic nanostructures.

RESULTS

Experimental Setup. A simplified description of the experimental setup is provided in Figure 1a. On the laser path, a radial polarization converter followed by a spatial filter with a 20-μm pinhole generates radially and azimuthally polarized light beams, which display doughnut-shape intensity profiles (Figure 1b). The linearly polarized Gaussian beam is obtained by bypassing the polarization converter. After a beam expander, an iris fixes the beam diameter to 5 mm, which results in a filling factor $D \approx 0.7$ of the objective back aperture. The incoming field couples to the sample via a 0.95-NA objective. The Stokes side of the inelastically scattered field is spectrally filtered before reaching the spectrometer.

The wavelength tunability of the Ti:Sapph laser source and the polarization modularity of our setup (see SI for details) enable a variety of different Raman excitation settings. The radial and azimuthal far fields correspond to superpositions of first-order Hermite-Gaussian modes ($HG_{mn}(x, y)$) $\boldsymbol{E}_R = HG_{10}(x, y)\boldsymbol{n}_x + HG_{01}(x, y)\boldsymbol{n}_y$ and $\boldsymbol{E}_A = HG_{10}(x, y)\boldsymbol{n}_y - HG_{01}(x, y)\boldsymbol{n}_x$, respectively, where $\boldsymbol{n}_i$ ($i = x, y$) are unit vectors perpendicular to the propagation direction. These traveling modes, solutions of the Helmholtz equation, belong to the set of cylindrical vector beams and are currently used in a variety of nano-optics applications.[43,44] Such beams feature position-dependent polarization and a singular point of zero intensity on the optical axis, giving them a characteristic doughnut-shaped intensity profile. In the same Hermite-Gaussian base, the linearly polarized Gaussian beams are defined as $\boldsymbol{E}_{Lx} = HG_{00}(x, y)\boldsymbol{n}_x$ and $\boldsymbol{E}_{Ly} = HG_{00}(x, y)\boldsymbol{n}_y$.

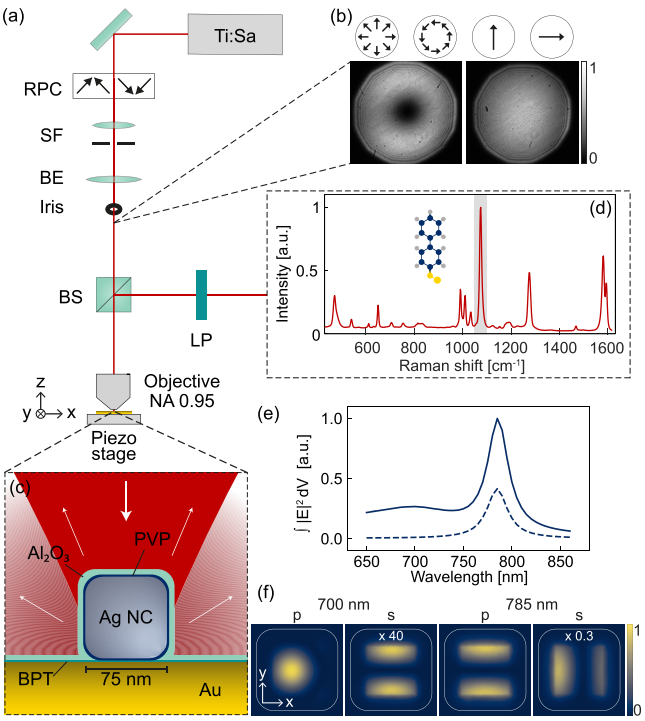

Figure 1. (a) Sketch of the experimental setup. RCP, Radial polarization converter; SP, spatial filter, BE, beam expander; BS, beam splitter; LP, long-pass filter. (b) Beam profiles after the iris for different laser polarizations. (c) Sketch of a single nanocavity being scanned across the excitation focal plane. (d) Acquired Raman spectrum for a particular sample position; the Stokes scattering intensity from the vibrational mode at ∼1075 cm^{-1} is integrated over the gray region for subsequent construction of excitation maps. (e) Finite element method (FEM) simulations of $|E|^2$ integrated over the gap region for *p*-polarized (solid line) and *s*-polarized (dashed line) plane-wave excitation at grazing incidence. (f) Near-field intensity distribution along the *xy* plane crossing the center of the gap for 700 and 785 nm excitation with *p* and *s* polarization. The simulations are realized for a gap size of 2.5 nm and rounding factor of 0.44 (see Supporting Information (SI)). The cube outline is indicated in white.

The sample is fixed on a piezo-stage that is finely scanned across the focal plane in *x* and *y* directions, for a fixed *z* position along the optical axis (see SI for details). The Raman-active nanocavities are fabricated on a template-stripped 150 nm thick gold film, on which biphenyl-4-thiol (BPT) molecules form a self-assembled monolayer (SAM) and 75 nm silver nanocubes (NC) are dropcasted (Figure 1c). The polyvinylpyrrolidone (PVP) ligand attached to the cubes (NanoXact by nanoComposix) contributes to the gap size. A 5 nm Al_2O_3 coating formed by atomic layer deposition (ALD) improves the stability of the nanostructures against oxidation and laser-induced damage.[45]

At each sample position, a cavity-enhanced Raman spectrum of the BPT molecules is acquired, as illustrated in Figure 1c. The three most intense peaks at 1075 cm^{-1}, 1280 cm^{-1}, and 1585 cm^{-1} correspond to the ring stretching, S−H stretching, and C−H stretching vibrational modes, respectively. In the following, we use the integrated intensity over the ring stretching peak as a function of the *x*, *y* coordinate of the sample scan to build near-field excitation maps (intensities of other vibrational modes are analyzed in the SI). We used a large enough slit opening at the spectrometer input to ensure that the detection efficiency was independent of sample

https://doi.org/10.1021/acs.nanolett.3c00561
Nano Lett. 2023, 23, 4885−4892

position over the range of the maps presented further. Consequently, we consider that the extracted intensity of the Raman signal is a faithful measure of the relative excitation efficiency when scanning the sample. We calibrated the wavelength- and polarization-dependent detection efficiency of the setup from the sample to the detector as well as the wavelength- and polarization-dependent transmission of the excitation path; see Figure S2 and accompanying discussion.

Theory of Polarization-Dependent Raman Signals. We briefly discuss how the enhancement of the Raman signal depends on the geometry of the nanocavity and on the excitation conditions (cf. near-field intensity simulations in Figure 1e,f). The considered NPoM geometry is expected to present one hybrid mode J_- at ∼700 nm and one transverse S_{11} mode at ∼785 nm. The mode J_- comes from the mixing of the transverse S_{02} and longitudinal L_{01} modes and has a prevalent longitudinal antenna polarization.[46] Note that the near-field polarization inside the nanogap is mostly longitudinal (along z) for all modes. As suggested by previous dark-field scattering studies,[20] the coupling of this NPoM mode to a linearly polarized beam impinging at grazing angle would be optimal for p polarization. Oppositely, s-polarized light would preferentially couple to the S_{11} mode.

Consider now the Raman signal caused by a single molecule located inside the gap, when the nanocavity position in the excitation field is $\boldsymbol{r}$. For a given excitation frequency ω_0 and polarization ϵ= R, A, Lx, Ly (radial, azimuthal, linear along x and y, respectively), the Stokes Raman power per unit of input power P_0 is proportional to

$$\frac{P_S(\boldsymbol{r}, \omega_0, \epsilon)}{P_0} \propto I_{gap}(\boldsymbol{r}, \omega_0, \epsilon) R_{zz}^2 F_{rad}(\omega_S) \quad (1)$$

where $R_{zz} = \boldsymbol{n}_z \cdot \boldsymbol{R} \cdot \boldsymbol{n}_z$ is the longitudinal component of the single-molecule Raman polarizability tensor $\boldsymbol{R}$ for the vibrational mode of interest (inside the gap the in-plane field is negligible in comparison to the out-of-plane field); $F_{rad}(\omega_S)$ is the radiative Purcell factor, which describes the out-coupling enhancement at the Stokes frequency $\omega_S = \omega_0 - \omega_\nu$ corresponding to the vibrational mode at ω_ν, and it depends on the full spectral response of the plasmonic cavity. The longitudinal field intensity inside the gap is given by

$$I_{gap}(\boldsymbol{r}, \omega_0, \epsilon) = I_{bg}^z(\boldsymbol{r}, \epsilon) K^z(\omega_0) + I_{bg}^{xy}(\boldsymbol{r}, \epsilon) K^{xy}(\omega_0) \quad (2)$$

where $I_{bg}(\boldsymbol{r}, \epsilon) = I_{bg}^z(\boldsymbol{r}, \epsilon) + I_{bg}^{xy}(\boldsymbol{r}, \epsilon)$ is the intensity profile of the background excitation field $\boldsymbol{E}_{bg}(\boldsymbol{r}, \epsilon) = \sum_i E_{bg}^i(\boldsymbol{r}, \epsilon) \boldsymbol{n}_i$ with $i = x, y, z$, such that

$$I_{bg}^z(\boldsymbol{r}, \epsilon) = |E_{bg}^z(\boldsymbol{r}, \epsilon)|^2$$

and

$$I_{bg}^{xy}(\boldsymbol{r}, \epsilon) = |E_{bg}^{xy}(\boldsymbol{r}, \epsilon)|^2 = |E_{bg}^x(\boldsymbol{r}, \epsilon)|^2 + |E_{bg}^y(\boldsymbol{r}, \epsilon)|^2$$

(see Figure 2a,c). The longitudinal (K^z) and transverse (K^{xy}) in-coupling enhancement factors depend on the exact position of the molecule inside the gap (and so does the Purcell factor) and can be estimated from electromagnetic simulations under linearly polarized plane wave excitation. When a molecular monolayer occupies the entire gap area, a proper computation of the Raman power should consider collective "bright" modes,[37] but this more advanced treatment is not necessary here since we do not consider power-dependent collective effects.[47] Apart from a different scaling factor, eq 1 remains valid.

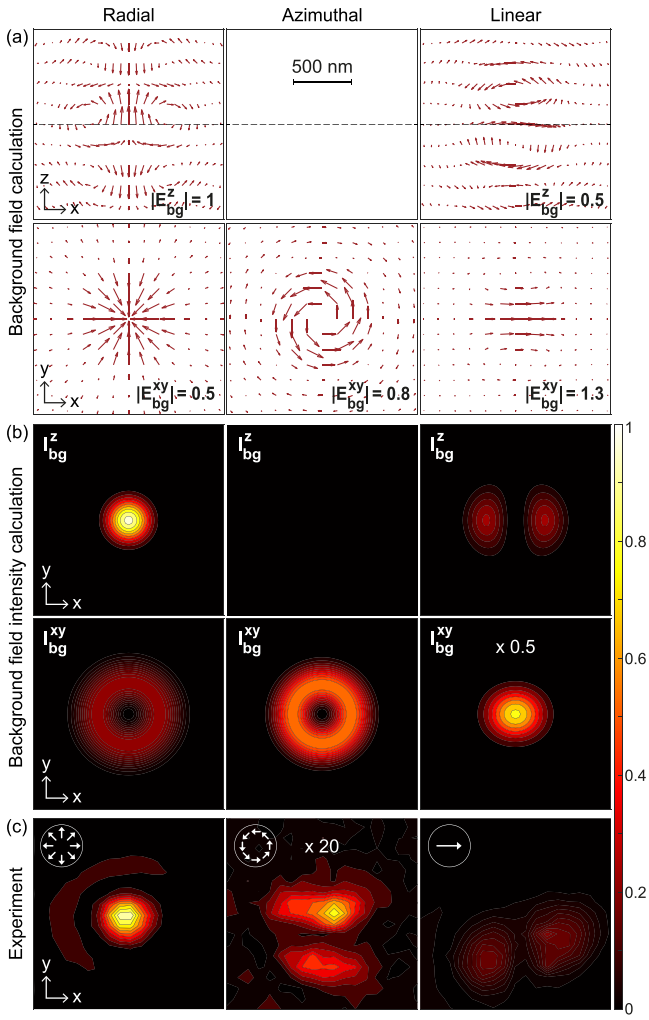

Figure 2. Comparison of experimental Raman intensity with calculated excitation fields near focus. (a) Computed background electric field in the xz and xy planes, where the dashed line represents the focal plane. In each panel, the maximum value of the longitudinal $E_{bg}^z(\boldsymbol{r}, \epsilon)$ or transverse $E_{bg}^{xy}(\boldsymbol{r}, \epsilon)$ field component is reported in relative units. (b) Corresponding longitudinal (z) and transverse (r) components of the background field intensity $I_{bg}(\boldsymbol{r}_0, \epsilon)$ (across the focal plane $z = 0$). All the simulations are realized by taking into account the specification of our objective, the filling factor D, and the experimental wavelength. (c) Measured maps of the Stokes intensity at 1075 cm^{-1} obtained with an excitation wavelength of 710 nm (SEM image of the nanocube in Figure S1). Some panels are rescaled in intensity when indicated.

The main conclusion is that eq 2 describes how the total emitted Raman power depends on the sample position for a given frequency and polarization of the excitation field through the distinct in-coupling enhancement factors for the longitudinal and transverse background field components. In particular, if the excitation frequency ω_0 is close to resonance with a longitudinal antenna mode, then $K^z(\omega_0) \gg K^{xy}(\omega_0)$ and the Raman signal will be strongest when the sample position $\boldsymbol{r}$ matches a maximum of $I_{bg}^z(\boldsymbol{r}, \epsilon)$; conversely, if ω_0 is close to resonance with a transverse antenna mode, then $K^z(\omega_0) \ll K^{xy}(\omega_0)$ and the Raman signal will be strongest when the sample position $\boldsymbol{r}$ matches a maximum of $I_{bg}^{xy}(\boldsymbol{r}, \epsilon)$. This discussion allows us to interpret the experimental confocal

https://doi.org/10.1021/acs.nanolett.3c00561
Nano Lett. 2023, 23, 4885−4892

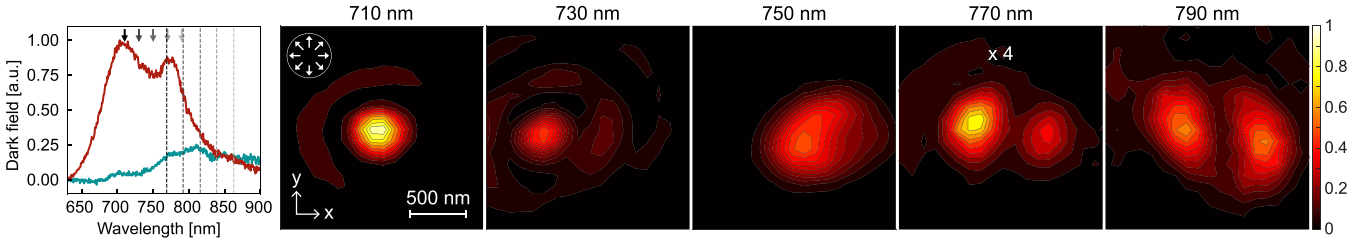

Figure 3. Wavelength sweep under radially polarized illumination. Left panel: Dark-field spectrum of the NCoM when excited with *s* (turquoise curve) and *p* (red curve) polarized light. Other panels: Measured maps of the Raman intensity at 1075 cm^{-1} obtained with different excitation wavelengths. Each excitation wavelength is indicated by an arrow in the dark-field plot, while the dashed line with the corresponding gray scale indicates the wavelength of the Raman mode at 1075 cm^{-1}.

Raman maps by connecting them to the near-field distribution of the focused excitation beam[48] and the transverse vs longitudinal nature of the antenna mode that is associated with each plasmonic gap mode.

Experimental Raman Maps of Individual Nanocavities. We excite a nanocube-on-mirror (NCoM) cavity (embedding BPT molecules) with the different light modes introduced earlier: $\boldsymbol{E}_R$, $\boldsymbol{E}_A$, $\boldsymbol{E}_{Lx}$, $\boldsymbol{E}_{Ly}$. Figure 2a shows the calculated local field components produced by these light modes close to the focus of the objective in the *xz* and *xy* planes. A Raman intensity map of the 1075 cm^{-1} vibrational mode excited at 710 nm (vacuum wavelength) is reported in Figure 2c. By comparing it with the numerically calculated intensity patterns $I_{bg}^{xy}(\boldsymbol{r}_0, \epsilon)$ and $I_{bg}^{z}(\boldsymbol{r}_0, \epsilon)$ (at the focal plane $z = 0$) plotted in Figure 2b, we find that for this excitation wavelength Raman scattering improves significantly when the NCoM cavity is positioned in a region where the background excitation field has the largest out-of-plane (longitudinal) component. Indeed, Raman intensity maps collected under radially ($\boldsymbol{E}_R$) and linearly ($\boldsymbol{E}_{Lx}$) polarized illuminations match well the calculated distribution of $I_{bg}^{z}(\boldsymbol{r}_0, \epsilon)$ (ϵ = R, Lx), both in their shapes and relative intensities. At the chosen excitation wavelength (~710 nm), our Raman maps thus clearly demonstrate the preferential coupling of the laser field to the longitudinally polarized J_- mode.

Since the focusing of the azimuthally ($\boldsymbol{E}_A$) polarized beam results in $I_{bg}^{z}(\boldsymbol{r}_0, A) = 0$ over the whole focal plane, Raman scattering can then only happen through the excitation of the far detuned S_{11} transverse mode, resulting in a much lower coupling efficiency and weaker Stokes signal. More quantitatively, we found that the ratio between the maximum Raman intensities with radial and azimuthal polarization (= 23.5) is comparable to the ratio of Stokes Raman powers numerically calculated via eq 1, taking into account the different positions of their maxima (= 32.6, see SI). The polarization of the outgoing field is not analyzed in these measurements, and it is in general different from the background polarization exciting the nanocavity. We therefore checked that our detection efficiency is largely polarization insensitive for ~710 nm excitation (Figure S2) so that we can safely attribute the change of Raman intensity to the change in input coupling efficiency.

Note that the experimental Raman map does not present a full ring pattern as expected for the transverse field of a focused azimuthally polarized beam. A first reason is the unbalanced superposition of $HG_{10}(x, y)\boldsymbol{n}_y$ and $HG_{01}(x, y)\boldsymbol{n}_x$ at the back aperture of the objective due to polarization-dependent transmission efficiency of some components (such as the beam splitter). We do measure that the *y* polarization is attenuated by almost 30% compared to the *x* component in the excitation path, altering the predicted ring pattern (see Figure S2). A second reason is that the nanocavity breaks the cylindrical symmetry and in general exhibits nondegenerate transverse resonances.

Altogether, these first results confirm that Raman intensity maps reveal the polarization-dependent near-field excitation efficiency of localized surface plasmon resonances and can be used to determine the nature of the antenna modes to which the laser preferentially couples at a particular wavelength.

Mode-Specific Coupling. We now demonstrate how the respective contributions of distinct nanocavity modes to the SERS signal can be identified and modified by tuning the wavelength and polarization of the incoming beam. We sweep the excitation wavelength under fixed $\boldsymbol{E}_R$ illumination on the same NCoM cavity. As shown in Figure 3, the single central lobe, consistent with input coupling to the longitudinal J_- mode at 710 nm, progressively transforms into two lobes as the excitation wavelength increases to 790 nm. This intensity pattern should be compared with the calculated spatial distribution of $I_{bg}^{z}(\boldsymbol{r}_0, R)$ in Figure 2. Here again, while we expect a ring pattern when the laser couples to the transverse S_{11} mode, the cylindrical symmetry is broken by the nanoparticle shape as well as the polarization-dependent transmission on the excitation path and results in a more efficient coupling to a particular transverse polarization, here close to the *x*-axis. Complementary data for different incoming light modes and other NCoMs are presented in the SI.

In Figure 4, we illustrate the use of our method on nanocavities with various nanoparticle shapes. Figure 4a presents data for another NCoM for which the polarization dependent dark-field scattering spectrum is inconclusive as to the nature of the gap modes. From the Raman intensity maps, a clear passage from longitudinal to transverse mode coupling is monitored under both radial and linear polarization. In this example, the superiority of the confocal scanning approach compared to polarized dark-field measurements is evident when it comes to determining the nature of the excited modes vs incoming wavelength.

Theoretical models and numerical studies have predicted how L_{01} and S_{11} modes of quasi-spherical NPoM undergo frequency crossing as a function of the size and shape of the bottom facet of the nanoparticle,[21,22] a parameter that cannot be easily controlled during fabrication nor be measured by existing nanoscopy techniques. Interestingly, our technique can efficiently discriminate these modes' contributions. In the case of the NPoM in Figure 4b, a single resonance appears in dark field: since the Raman intensity maps at 750 nm excitation indicates a preferential longitudinal input coupling, we can associate this resonance to the longitudinal L_{01} mode rather

https://doi.org/10.1021/acs.nanolett.3c00561
Nano Lett. 2023, 23, 4885−4892

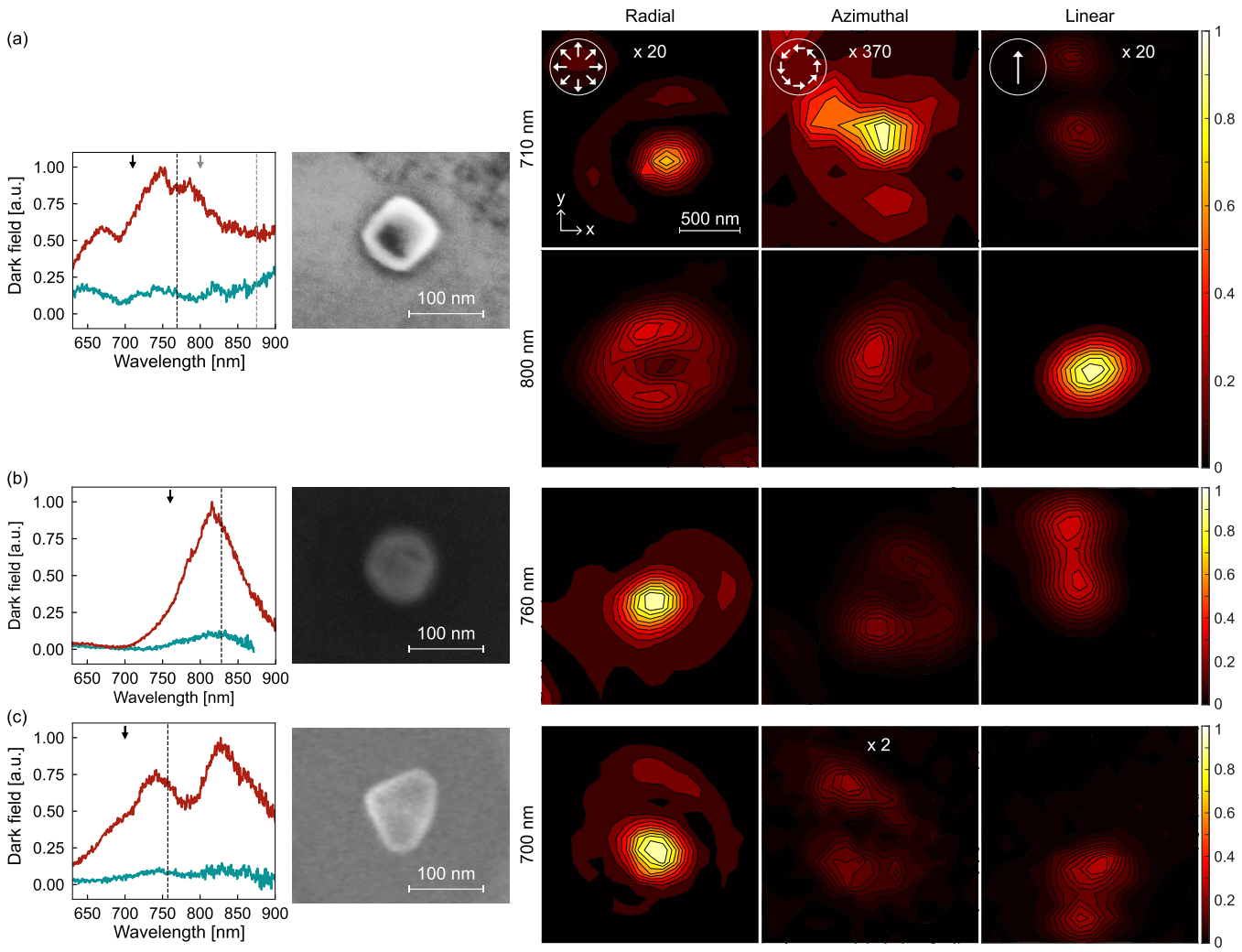

Figure 4. Comparison of different NPoM nanocavities: (a) 75 nm ALD-coated silver nanocube (NanoXact by nanoComposix), (b) 80 nm gold nanosphere (by BBI solutions), and (c) triangular gold particle found in a sample of gold nanocubes (A1C-80 by Nanopartz).

than S_{11}. Finally, Figure 4c corroborates the validity of the technique for a more irregularly shaped NPoM, where we can evidence more efficient coupling to a longitudinally polarized mode around 700 nm. For completeness, we also present in the SI the Raman maps of larger nanospheres (150 nm diameter) decorated with BPT molecules on a glass substrate for different excitation beams. It must be highlighted that our technique could straightforwardly be applied for the characterization of a large variety of nanostructures, including other mirror-based nanocavities (dimer-on-mirror,[49] magnetic resonances,[50] etc.), and could be performed using a variety of signals. We illustrate this flexibility in the SI by performing complementary photoluminescence maps of our gold nanocavities under radial and azimuthal illumination.

CONCLUSION

We demonstrated mode-selective laser excitation of nanoparticle-on-mirror systems using a simple technique based on the Raman signal from embedded molecules. By performing confocal Raman mapping under radial, azimuthal, and linear polarization for different laser wavelengths, we could unambiguously determine the longitudinal vs transverse polarization of the antenna mode most efficiently coupled to the incoming beam and show the transition from one mode to another on a singular nanostructure as the laser wavelength is tuned. Our method vividly reveals the distinct nature of ultraconfined modes most efficiently excited at particular wavelengths and proves to be a versatile nanoscopy tool able to address irregular nanocavities. Using faster acquisition rates, the method could also be extended to interrogate unstable picocavities.[51] Thanks to its uncomplicated implementation, our tool can be combined with other nanoscopy techniques to simultaneously acquire *k*-space[52,53] or phase information.[54] Other brighter signals emanating from resonant Raman scattering[55,56] or fluorescence[1] could be used as a local probe to learn more and control better their interaction with gap modes, extending on the seminal studies that introduced the technique for focused laser beams.[57−59]

This work is a first step toward a precise and quantitative estimate of input coupling rates between far-field radiation and nanocavity modes. These are key quantities in several plasmonic sensing schemes[34,35] and are essential for accurate modeling and testing of novel predictions of molecular cavity optomechanics such as the appearance of dynamical back-action and optical-spring effects at the molecular level.[37,60] Our results also pave the way for extended studies and optimization of input coupling rates for rapidly evolving hot-spots[51,61,62] with the help of adaptive-optics illumination.[63] More directly,

https://doi.org/10.1021/acs.nanolett.3c00561
Nano Lett. 2023, 23, 4885−4892

we showed that the control of the incoming beam allows to select the gap mode contributing to the targeted light-matter interaction and enables pushing further the sensitivity of nanodevices using ultraconfined cavity modes.

■ ASSOCIATED CONTENT

Data Availability Statement

The data, plotting, and calibration routines as well as the numerical tools underlying this study are openly available in a Zenodo repository at 10.5281/zenodo.7829144.

Supporting Information

The Supporting Information is available free of charge at https://pubs.acs.org/doi/10.1021/acs.nanolett.3c00561.

Description of near-field FEM simulations, background fields numerical calculations and optical setup; methods for Raman maps acquisition and setup calibration with additional considerations of polarization imbalance; photoluminescence maps, Raman maps for other BPT vibrational modes, 150 nm NP on glass Raman maps, comparison of Raman signals in counts unit, Raman maps superimposed with calculated background fields in the focal plane, complete wavelength and polarization sweep on a NCoM, effect of the plasmonic response on wavelength-dependent SERS measurements (PDF)

■ AUTHOR INFORMATION

Corresponding Authors

Christophe Galland − *Institute of Physics, École Polytechnique Fédérale de Lausanne (EPFL), CH-1015 Lausanne, Switzerland;* orcid.org/0000-0001-5627-0796; Email: chris.galland@epfl.ch

Philippe Roelli − *Nano-optics Group, CIC nanoGUNE, E-20018 Donostia-San Sebastián, Spain;* orcid.org/0000-0002-1582-2301; Email: p.roelli@nanogune.eu

Authors

Valeria Vento − *Institute of Physics, École Polytechnique Fédérale de Lausanne (EPFL), CH-1015 Lausanne, Switzerland;* orcid.org/0000-0003-3591-8682

Sachin Verlekar − *Institute of Physics, École Polytechnique Fédérale de Lausanne (EPFL), CH-1015 Lausanne, Switzerland*

Complete contact information is available at: https://pubs.acs.org/10.1021/acs.nanolett.3c00561

Notes

The authors declare no competing financial interest.

■ ACKNOWLEDGMENTS

This project has received funding from the Swiss National Science Foundation (Grant Nos. 170684, 198898, and 206926) and from the European Union's Horizon 2020 research and innovation program under Grant Agreement No. 820196 (ERC CoG QTONE). The authors thank Huatian Hu for assistance with numerical simulations and Prof. Kippenberg for offering laboratory access.

■ REFERENCES

(1) Chikkaraddy, R.; de Nijs, B.; Benz, F.; Barrow, S. J.; Scherman, O. A.; Rosta, E.; Demetriadou, A.; Fox, P.; Hess, O.; Baumberg, J. J. Single-molecule strong coupling at room temperature in plasmonic nanocavities. *Nature* **2016**, *535*, 127.

(2) Xiong, X.; Kongsuwan, N.; Lai, Y.; Png, C. E.; Wu, L.; Hess, O. Room-temperature plexcitonic strong coupling: Ultrafast dynamics for quantum applications. *Appl. Phys. Lett.* **2021**, *118*, 130501.

(3) Heintz, J.; Markešević, N.; Gayet, E. Y.; Bonod, N.; Bidault, S. Few-Molecule Strong Coupling with Dimers of Plasmonic Nanoparticles Assembled on DNA. *ACS Nano* **2021**, *15*, 14732.

(4) Liu, X.; Yi, J.; Yang, S.; Lin, E.-C.; Zhang, Y.-J.; Zhang, P.; Li, J.-F.; Wang, Y.; Lee, Y.-H.; Tian, Z.-Q.; Zhang, X. Nonlinear valley phonon scattering under the strong coupling regime. *Nat. Mater.* **2021**, *20*, 1210.

(5) Bylinkin, A.; Schnell, M.; Autore, M.; Calavalle, F.; Li, P.; Taboada-Gutièrrez, J.; Liu, S.; Edgar, J. H.; Casanova, F.; Hueso, L. E.; Alonso-Gonzalez, P.; Nikitin, A. Y.; Hillenbrand, R. Real-space observation of vibrational strong coupling between propagating phonon polaritons and organic molecules. *Nat. Photonics* **2021**, *15*, 197.

(6) Zhang, R.; Zhang, Y.; Dong, Z. C.; Jiang, S.; Zhang, C.; Chen, L. G.; Zhang, L.; Liao, Y.; Aizpurua, J.; Luo, Y.; Yang, J. L.; Hou, J. G. Chemical mapping of a single molecule by plasmon-enhanced Raman scattering. *Nature* **2013**, *498*, 82.

(7) Lee, J.; Crampton, K. T.; Tallarida, N.; Apkarian, V. A. Visualizing vibrational normal modes of a single molecule with atomically confined light. *Nature* **2019**, *568*, 78.

(8) Sun, M.; Zhang, Z.; Zheng, H.; Xu, H. In-situ plasmon-driven chemical reactions revealed by high vacuum tip-enhanced Raman Spectroscopy. *Sci. Rep* **2012**, *2*, 647.

(9) Kern, J.; Kullock, R.; Prangsma, J.; Emmerling, M.; Kamp, M.; Hecht, B. Electrically driven optical antennas. *Nature Photon* **2015**, *9*, 582.

(10) Celebrano, M.; Wu, X.; Baselli, M.; Großmann, S.; Biagioni, P.; Locatelli, A.; De Angelis, C.; Cerullo, G.; Osellame, R.; Hecht, B.; Duò, L.; Ciccacci, F.; Finazzi, M. Mode matching in multiresonant plasmonic nanoantennas for enhanced second harmonic generation. *Nat. Nanotechnol.* **2015**, *10*, 412.

(11) Hoang, T. B.; Akselrod, G. M.; Mikkelsen, M. H. Ultrafast Room-Temperature Single Photon Emission from Quantum Dots Coupled to Plasmonic Nanocavities. *Nano Lett.* **2016**, *16*, 270.

(12) Chen, W.; Roelli, P.; Hu, H.; Verlekar, S.; Amirtharaj, S. P.; Barreda, A. I.; Kippenberg, T. J.; Kovylina, M.; Verhagen, E.; Martínez, A.; Galland, C. Continuous-wave frequency upconversion with a molecular optomechanical nanocavity. *Science* **2021**, *374*, 1264.

(13) Li, G.-C.; Zhang, Q.; Maier, S. A.; Lei, D. Plasmonic particle-on-film nanocavities: A versatile platform for plasmon-enhanced spectroscopy and photochemistry. *Nanophotonics* **2018**, *7*, 1865.

(14) Baumberg, J. J.; Aizpurua, J.; Mikkelsen, M. H.; Smith, D. R. Extreme nanophotonics from ultrathin metallic gaps. *Nat. Mater.* **2019**, *18*, 668.

(15) Aravind, P. K.; Rendell, R. W.; Metiu, H. A new geometry for field enhancement in surface-enhanced spectroscopy. *Chem. Phys. Lett.* **1982**, *85*, 396.

(16) Lee, S. Nanoparticle-on-mirror cavity: a historical view across nanophotonics and nanochemistry. *J. Korean Phys. Soc.* **2022**, *81*, 502.

(17) Chen, W.; Zhang, S.; Kang, M.; Liu, W.; Ou, Z.; Li, Y.; Zhang, Y.; Guan, Z.; Xu, H. Probing the limits of plasmonic enhancement using a two-dimensional atomic crystal probe. *Light: Science & Applications* **2018**, *7*, 56.

(18) Lassiter, J. B.; McGuire, F.; Mock, J. J.; Ciracì, C.; Hill, R. T.; Wiley, B. J.; Chilkoti, A.; Smith, D. R. Plasmonic Waveguide Modes of Film-Coupled Metallic Nanocubes. *Nano Lett.* **2013**, *13*, 5866.

(19) Tserkezis, C.; Esteban, R.; Sigle, D. O.; Mertens, J.; Herrmann, L. O.; Baumberg, J. J.; Aizpurua, J. Hybridization of plasmonic antenna and cavity modes: Extreme optics of nanoparticle-on-mirror nanogaps. *Phys. Rev. A* **2015**, *92*, 053811.

(20) Chikkaraddy, R.; Zheng, X.; Benz, F.; Brooks, L. J.; de Nijs, B.; Carnegie, C.; Kleemann, M.-E.; Mertens, J.; Bowman, R. W.; Vandenbosch, G. A. E.; Moshchalkov, V. V.; Baumberg, J. J. How Ultranarrow Gap Symmetries Control Plasmonic Nanocavity Modes: From Cubes to Spheres in the Nanoparticle-on-Mirror. *ACS Photonics* **2017**, *4*, 469.

(21) Kongsuwan, N.; Demetriadou, A.; Horton, M.; Chikkaraddy, R.; Baumberg, J. J.; Hess, O. Plasmonic Nanocavity Modes: From Near-Field to Far-Field Radiation. *ACS Photonics* **2020**, *7*, 463.
(22) Elliott, E.; Bedingfield, K.; Huang, J.; Hu, S.; de Nijs, B.; Demetriadou, A.; Baumberg, J. J. Fingerprinting the Hidden Facets of Plasmonic Nanocavities. *ACS Photonics* **2022**, *9*, 2643.
(23) Hughes, S.; Settineri, A.; Savasta, S.; Nori, F. Resonant Raman scattering of single molecules under simultaneous strong cavity coupling and ultrastrong optomechanical coupling in plasmonic resonators: Phonon-dressed polaritons. *Phys. Rev. B* **2021**, *104*, 045431.
(24) Wu, T.; Gurioli, M.; Lalanne, P. Nanoscale Light Confinement: The Q's and V's. *ACS Photonics* **2021**, *8*, 1522.
(25) Li, C.-Y.; Duan, S.; Wen, B.-Y.; Li, S.-B.; Kathiresan, M.; Xie, L.-Q.; Chen, S.; Anema, J. R.; Mao, B.-W.; Luo, Y.; Tian, Z.-Q.; Li, J.-F. Observation of inhomogeneous plasmonic field distribution in a nanocavity. *Nat. Nanotechnol.* **2020**, *15*, 922.
(26) Long, J.; Yi, H.; Li, H.; Lei, Z.; Yang, T. Reproducible Ultrahigh SERS Enhancement in Single Deterministic Hotspots Using Nanosphere-Plane Antennas Under Radially Polarized Excitation. *Sci. Rep* **2016**, *6*, 33218.
(27) Fulmes, J.; Gollmer, D. A.; Jäger, S.; Schäfer, C.; Horrer, A.; Zhang, D.; Adam, P.-M.; Meixner, A. J.; Kern, D. P.; Fleischer, M. Mapping the electric field distribution of tightly focused cylindrical vector beams with gold nanorings. *Opt. Express* **2018**, *26*, 14982.
(28) Shang, W.; Xiao, F.; Zhu, W.; Han, L.; Mei, T.; Zhao, J. Characterizing localized surface plasmon resonances using focused radially polarized beam. *Appl. Opt.* **2019**, *58*, 5812.
(29) Grosche, S.; Hünermann, R.; Sarau, G.; Christiansen, S.; Boyd, R. W.; Leuchs, G.; Banzer, P. Towards polarization-based excitation tailoring for extended Raman spectroscopy. *Opt. Express* **2020**, *28*, 10239.
(30) Tang, P.; Xing, X.; Liu, S.; Cheng, W.; Lu, X.; Zhong, L. Plasmonic Particle-on-Film Nanocavity in Tightly Focused Vector Beam: a Full-Wave Theoretical Analysis from Near-Field Enhancement to Far-Field Radiation. *Plasmonics* **2021**, *16*, 215.
(31) Esteban, R.; Aizpurua, J.; Bryant, G. W. Strong coupling of single emitters interacting with phononic infrared antennae. *New J. Phys.* **2014**, *16*, 013052.
(32) Sánchez-Barquilla, M.; Silva, R. E. F.; Feist, J. Cumulant expansion for the treatment of light−matter interactions in arbitrary material structures. *J. Chem. Phys.* **2020**, *152*, 034108.
(33) Liu, N.; Langguth, L.; Weiss, T.; Kästel, J.; Fleischhauer, M.; Pfau, T.; Giessen, H. Plasmonic analogue of electromagnetically induced transparency at the Drude damping limit. *Nat. Mater.* **2009**, *8*, 758.
(34) Adato, R.; Artar, A.; Erramilli, S.; Altug, H. Engineered Absorption Enhancement and Induced Transparency in Coupled Molecular and Plasmonic Resonator Systems. *Nano Lett.* **2013**, *13*, 2584.
(35) Neuman, T.; Huck, C.; Vogt, J.; Neubrech, F.; Hillenbrand, R.; Aizpurua, J.; Pucci, A. Importance of Plasmonic Scattering for an Optimal Enhancement of Vibrational Absorption in SEIRA with Linear Metallic Antennas. *J. Phys. Chem. C* **2015**, *119*, 26652.
(36) Neubrech, F.; Huck, C.; Weber, K.; Pucci, A.; Giessen, H. Surface-Enhanced Infrared Spectroscopy Using Resonant Nanoantennas. *Chem. Rev.* **2017**, *117*, 5110.
(37) Roelli, P.; Galland, C.; Piro, N.; Kippenberg, T. J. Molecular cavity optomechanics as a theory of plasmon-enhanced Raman scattering. *Nat. Nanotechnol.* **2016**, *11*, 164.
(38) Schmidt, M. K.; Esteban, R.; González-Tudela, A.; Giedke, G.; Aizpurua, J. Quantum Mechanical Description of Raman Scattering from Molecules in Plasmonic Cavities. *ACS Nano* **2016**, *10*, 6291.
(39) Schmidt, M. K.; Esteban, R.; Benz, F.; Baumberg, J. J.; Aizpurua, J. Linking classical and molecular optomechanics descriptions of SERS. *Faraday Discuss.* **2017**, *205*, 31.
(40) Roelli, P.; Martin-Cano, D.; Kippenberg, T. J.; Galland, C. Molecular Platform for Frequency Upconversion at the Single-Photon Level. *Physical Review X* **2020**, *10*, 031057.
(41) Esteban, R.; Baumberg, J. J.; Aizpurua, J. Molecular Optomechanics Approach to Surface-Enhanced Raman Scattering. *Acc. Chem. Res.* **2022**, *55*, 1889.
(42) Primo, A. G.; Carvalho, N. C.; Kersul, C. M.; Frateschi, N. C.; Wiederhecker, G. S.; Alegre, T. P. M. Quasinormal-Mode Perturbation Theory for Dissipative and Dispersive Optomechanics. *Phys. Rev. Lett.* **2020**, *125*, 233601.
(43) Züchner, T.; Failla, A. V.; Meixner, A. J. Light Microscopy with Doughnut Modes: A Concept to Detect, Characterize, and Manipulate Individual Nanoobjects. *Angew. Chem., Int. Ed.* **2011**, *50*, 5274.
(44) Rosales-Guzmán, C.; Ndagano, B.; Forbes, A. A review of complex vector light fields and their applications. *J. Opt.* **2018**, *20*, 123001.
(45) Chen, W.; Zhang, S.; Deng, Q.; Xu, H. Probing of subpicometer vertical differential resolutions using cavity plasmons. *Nat. Commun.* **2018**, *9*, 801.
(46) Zhang, C.; Hugonin, J.-P.; Greffet, J.-J.; Sauvan, C. Surface Plasmon Polaritons Emission with Nanopatch Antennas: Enhancement by Means of Mode Hybridization. *ACS Photonics* **2019**, *6*, 2788.
(47) Zhang, Y.; Aizpurua, J.; Esteban, R. Optomechanical Collective Effects in Surface-Enhanced Raman Scattering from Many Molecules. *ACS Photonics* **2020**, *7*, 1676.
(48) Liu, Q.; Ge, D.; Wackenhut, F.; Coplan, C. D.; Cherqui, C.; Brecht, M.; Lin, X.-M.; Schatz, G. C.; Schaller, R. D.; Adam, P.-M.; Bachelot, R.; Meixner, A. J. Revealing the Three-Dimensional Orientation and Interplay between Plasmons and Interband Transitions for Single Gold Bipyramids by Photoluminescence Excitation Pattern Imaging. *J. Phys. Chem. C* **2021**, *125*, 26978.
(49) Li, G.-C.; Zhang, Y.-L.; Jiang, J.; Luo, Y.; Lei, D. Y. Metal-Substrate-Mediated Plasmon Hybridization in a Nanoparticle Dimer for Photoluminescence Line-Width Shrinking and Intensity Enhancement. *ACS Nano* **2017**, *11*, 3067.
(50) Chen, S.; Zhang, Y.; Shih, T.-M.; Yang, W.; Hu, S.; Hu, X.; Li, J.; Ren, B.; Mao, B.; Yang, Z.; Tian, Z. Plasmon-Induced Magnetic Resonance Enhanced Raman Spectroscopy. *Nano Lett.* **2018**, *18*, 2209.
(51) Benz, F.; Schmidt, M. K.; Dreismann, A.; Chikkaraddy, R.; Zhang, Y.; Demetriadou, A.; Carnegie, C.; Ohadi, H.; Nijs, B. d.; Esteban, R.; Aizpurua, J.; Baumberg, J. J. Single-molecule optomechanics in "picocavities. *Science* **2016**, *354*, 726.
(52) Lieb, M. A.; Zavislan, J. M.; Novotny, L. Single-molecule orientations determined by direct emission pattern imaging. *JOSA B* **2004**, *21*, 1210.
(53) Röhrich, R.; Hoekmeijer, C.; Osorio, C. I.; Koenderink, A. F. Quantifying single plasmonic nanostructure far-fields with interferometric and polarimetric k-space microscopy. *Light: Science & Applications* **2018**, *7*, 65.
(54) Bauer, T.; Orlov, S.; Peschel, U.; Banzer, P.; Leuchs, G. Nanointerferometric amplitude and phase reconstruction of tightly focused vector beams. *Nature Photon* **2014**, *8*, 23.
(55) Haynes, C. L.; Van Duyne, R. P. Plasmon-Sampled Surface-Enhanced Raman Excitation Spectroscopy. *J. Phys. Chem. B* **2003**, *107*, 7426.
(56) Itoh, T.; Yamamoto, Y. S. Between plasmonics and surface-enhanced resonant Raman spectroscopy: toward single-molecule strong coupling at a hotspot. *Nanoscale* **2021**, *13*, 1566.
(57) Sick, B.; Hecht, B.; Novotny, L. Orientational Imaging of Single Molecules by Annular Illumination. *Phys. Rev. Lett.* **2000**, *85*, 4482.
(58) Novotny, L.; Beversluis, M. R.; Youngworth, K. S.; Brown, T. G. Longitudinal Field Modes Probed by Single Molecules. *Phys. Rev. Lett.* **2001**, *86*, 5251.
(59) Failla, A. V.; Qian, H.; Qian, H.; Hartschuh, A.; Meixner, A. J. Orientational Imaging of Subwavelength Au Particles with Higher Order Laser Modes. *Nano Lett.* **2006**, *6*, 1374.
(60) Jakob, L. A., Deacon, W. M., Zhang, Y., de Nijs, B., Pavlenko, E., Hu, S., Carnegie, C., Neuman, T., Esteban, R., Aizpurua, J., Baumberg, J. J. Softening molecular bonds through the giant

https://doi.org/10.1021/acs.nanolett.3c00561
Nano Lett. 2023, 23, 4885−4892

optomechanical spring effect in plasmonic nanocavities. *arXiv:2204.09641* 2022. DOI: 10.48550/arXiv.2204.09641
(61) Lindquist, N. C.; de Albuquerque, C. D. L.; Sobral-Filho, R. G.; Paci, I.; Brolo, A. G. High-speed imaging of surface-enhanced Raman scattering fluctuations from individual nanoparticles. *Nat. Nanotechnol.* **2019**, *14*, 981.
(62) Chen, W.; Roelli, P.; Ahmed, A.; Verlekar, S.; Hu, H.; Banjac, K.; Lingenfelder, M.; Kippenberg, T. J.; Tagliabue, G.; Galland, C. Intrinsic luminescence blinking from plasmonic nanojunctions. *Nat. Commun.* **2021**, *12*, 2731.
(63) Lee, D. Y.; Park, C.; Choi, J.; Koo, Y.; Kang, M.; Jeong, M. S.; Raschke, M. B.; Park, K.-D. Adaptive tip-enhanced nano-spectroscopy. *Nat. Commun.* **2021**, *12*, 3465.

https://doi.org/10.1021/acs.nanolett.3c00561
Nano Lett. 2023, 23, 4885−4892